NIH Public Access
Author Manuscript
Magn Reson Med. Author manuscript; available in PMC 2009 September 1.

Published in final edited form as:
Magn Reson Med. 2008 October ; 60(4): 834–841. doi:10.1002/mrm.21714.

An Investigation of Optimizing and Translating pH-Sensitive Pulsed-Chemical Exchange Saturation Transfer (CEST) Imaging to a 3 T Clinical Scanner

Phillip Zhe Sun[1,*], **Thomas Benner**[1], **Ashok Kumar**[1], and **A Gregory Sorensen**[1]
[1]Athinoula A. Martinos Center for Biomedical Imaging, Massachusetts General Hospital, Department of Radiology and Harvard Medical School, Charlestown, MA 02129

Abstract

Chemical exchange saturation transfer (CEST) MRI provides a sensitive detection mechanism that allows characterization of dilute labile protons usually undetectable by conventional MRI. Particularly, amide proton transfer (APT) imaging, a variant of CEST MRI, has been shown capable of detecting ischemic acidosis, and may serve as a surrogate metabolic imaging marker. For pre-clinical CEST imaging, continuous-wave (CW) RF irradiation is often applied so that the steady state CEST contrast can be reached. On clinical scanners, however, specific absorption rate (SAR) limit and hardware preclude the use of CW irradiation, and instead require an irradiation scheme of repetitive RF pulses (pulsed-CEST imaging). In this work, CW- and pulsed-CEST MRI were systematically compared using a tissue-like pH phantom on an imager capable of both CW and pulsed RF irradiation schemes. The results showed that the maximally obtainable pulsed-CEST contrast is about 95% of CW-CEST contrast, and their optimal RF irradiation powers are equal. Moreover, the pulsed-CEST sequence was translated to a 3 T clinical scanner and detected pH contrast from the labile creatine amine groups (1.9 ppm). Furthermore, pilot endogenous APT imaging of normal human volunteers was demonstrated, warranting future APT MRI of stroke patients to elucidate its diagnostic value.

Keywords

Amide Proton Transfer (APT); Chemical Exchange Saturation Transfer (CEST); Magnetic Resonance Imaging (MRI); Magnetization Transfer (MT); pH

1. INTRODUCTION

In chemical exchange saturation transfer (CEST) imaging, bulk water magnetization is attenuated through its magnetization exchange with saturated labile protons, therefore making MRI, which usually detects bulk water only, sensitive to properties of dilute labile groups (1-4). Because chemical exchange is pH-dependent, CEST imaging may be applied to monitor microenvironment pH (5-7). In fact, amide proton transfer (APT) imaging, a variant of CEST imaging, has been shown capable of detecting tissue acidosis during acute stroke (8-10). Whereas perfusion and diffusion MRI is increasingly utilized to image acute ischemia and help guide stroke treatment, in particular for patients admitted to hospitals beyond the conventional thrombolytic window, it appears to have some limitations (11-13). Specifically, perfusion MRI overestimates tissue susceptible to stroke, while the tissue

*Corresponding authors: Phillip Zhe Sun, PhD, Rm 2301, 149 13th street, Athinoula A. Martinos Center for Biomedical Imaging, Department of Radiology, Massachusetts General Hospital, Harvard Medical School, Charlestown, MA 02129, E-mail: pzhesun@nmr.mgh.harvard.edu, Phone: 617-726-4060, Fax: 617-726-7422

NIH-PA Author Manuscript
NIH-PA Author Manuscript
NIH-PA Author Manuscript

NIH-PA Author Manuscript

NIH-PA Author Manuscript

NIH-PA Author Manuscript

outcome of the diffusion MRI lesion is heterogeneous. Portions of acute diffusion lesion may be reversed if promptly reperfused, suggesting that it may contain reversibly damaged ischemic tissue (14,15). While on the other hand, the final infarction area is often larger than the acute diffusion MRI lesion, which suggests that diffusion MRI may miss some irreversibly damaged tissue. Because maintenance of tissue metabolic energy is crucial to cell viability, markers of abnormal energy metabolism such as depletion of adenosine triphosphate (ATP), abnormal oxygen extraction ratio (OER), and tissue acidosis have been postulated capable of specifically highlighting ischemic tissue at risk to infarction (ischemic penumbra) (16-19). Thus, a non-invasive metabolic imaging technique, such as the proposed pH-weighted APT MRI, may complement the commonly used perfusion and diffusion MRI for more accurate characterization of ischemic penumbra (20,21).

Conventionally, a continuous-wave (CW) RF pulse of a few seconds is applied to saturate exchangeable protons for steady state CEST contrast. For labile protons well separated from bulk water frequency, the steady state CEST contrast can be described using a simplified 2-pool exchange model (22,23). However, for diamagnetic CEST imaging, the obtainable CEST contrast also depends on the RF irradiation/labeling scheme, particularly, the power of the irradiation RF. It is so because chemical shifts for diamagnetic labile groups are usually close to the bulk water resonance (within ~5 ppm), and therefore, the bulk water magnetization may be directly saturated by the irradiation RF pulse (spillover effects) (24). In order to delineate non-specific concomitant spillover effects from CEST contrast, an empirical solution has been derived that decomposes the experimentally obtained CEST ratio (CESTR) into a product of ideal CEST contrast, labeling coefficient and spillover factor (25). Given that CEST contrast and spillover effects vary differently with RF irradiation power, it has been shown that there exists an optimal RF power that can maximize the CEST contrast (25,26). For in vivo APT imaging, however, there are additional concomitant magnetization transfer (MT) effects between semisolid macromolecules and bulk water, and thus, it is even more complex to describe. Recently, Sun et al. proposed a dual 2-pool exchange model that provides simple yet reasonably accurate description of *in vivo* APT imaging, and quantified the endogenous amide proton concentration (10). Because pH is a key physiological parameter that changes in response to abnormal tissue energy metabolism, it may be important to translate pH-sensitive APT imaging to the clinic for better delineation of ischemic tissue to guide stroke therapeutics (17,27). However, due to specific absorption rate (SAR) limit and hardware design, the commonly used CW RF irradiation scheme is not applicable on clinical scanners, and an irradiation scheme of repetitive short RF irradiation pulses (pulsed-CEST imaging) must be chosen instead. Because the equivalent power and saturation bandwidth of repetitive RF pulse and CW irradiation are different; it is not certain whether the empirical solution derived for steady state CW-CEST imaging is suitable to describe and optimize pulsed-CEST imaging. In addition, the analytical solution for 2-pool or 3-pool chemical exchange model at non-steady state is very cumbersome at best, while it provides little insight. Considering that the endogenous pH-weighted APT contrast during acute stroke is only about 3%, it is crucial to optimize pulsed-CEST MRI before translating it for routine stroke exam (10).

In this study, we first characterized a tissue-like pH phantom on a high-field animal imager, and obtained its chemical exchange rate using numerical fitting of z-spectra obtained with CW-CEST imaging (26,28). We then compared CW- and pulsed-CEST imaging by measuring the CEST contrast while the irradiation RF power was systematically varied from weak (sub-μT) to strong (a few μT). The results showed that the optimal RF power for CW- and pulsed-CEST imaging is approximately equal, and so is the maximally obtainable CEST contrast. In addition, we implemented the pulsed-CEST imaging sequence on a 3 T clinical scanner and demonstrated that it can detect pH difference from the tissue-like pH phantom.

NIH-PA Author Manuscript

NIH-PA Author Manuscript

NIH-PA Author Manuscript

Furthermore, we obtained pilot pulsed-APT images from normal human volunteers, warranting future APT MRI of acute stroke patients to elucidate its diagnostic value.

2. MATERIALS AND METHODS

2.1. PHANTOM PREPARATION

Tissue-like pH phantoms were prepared as we described previously (28). Briefly, 3% agarose gel (w/w) was prepared by adding low-gelling point agarose (Sigma Aldrich, St Louis, MO) to filtered and deionized water (Millipore, Billerica, MA), and mixing well. The solution was then heated to the boiling point and immersed into a water bath preset at 46°C (Cole-Parmer, Vernon Hills, IL). After 15 minutes, creatine (Sigma Aldrich, St Louis, MO) was added to reach a concentration of 50 mM, and the mixture was vortexed. The pH was then titrated to 5.2, 6.0 and 6.4 at 46°C, respectively (EuTech Instrument, Singapore). It is useful to note that slightly acidic pH values were used so that their chemical exchange rates are comparable with that found for in vivo (8,10). In addition, the creatine concentration is chosen so the labile proton content is approximately equal to that of cerebral tissue (8,10,28). Solutions at pH of 5.2 and 6.0 were separately transferred into two centrifuge tubes, capped, sealed and inserted into a 50 ml Falcon tube. Solution at pH of 6.4 was then poured into the 50ml Falcon tube, filling the space surrounding the two centrifuge tubes inside. Afterward, the triple gel phantom was removed from the water bath and left at room temperature to solidify before experiments.

Additional gel-based phantoms (3% agarose gel and 50 mM creatine) were prepared for MRI at 3 Tesla, following the same protocol described above. The pH was titrated to 5.3, 5.9 and 6.5, and transferred into three 50 ml Falcon tubes. In addition, 50 mM creatine solution at pH of 5.8 was prepared and added to another 50 ml Falcon tube. The four Falcon tubes were bound together and transferred into a container (~ 140 × 140 × 200 mm) filled with 1 mM $CuSO_5 \cdot 5H_2O$ (Sigma Aldrich, St Louis, MO) solution. In addition, two acrylic tubes were inserted to position the quadruple pH phantom approximately at the iso-center for improved B_0 field homogeneity. Four normal volunteers (mean age = 33 ± 5 years, Male=3, Female=1) were enrolled in the scan. The study was approved by Partners HealthCare research review board, and signed consent forms were obtained prior to MRI scan. One subject was removed from data analysis due to severe motion artifacts.

2.2. MRI

The triple gel phantom was imaged on a 9.4T Bruker Biospec imager (Bruker Biospec, Billerica mA) at room temperature. A volume RF coil with inner diameter (ID) of 70 mm (Bruker Biospin, Billerica, MA) was used for the experiment. The main magnetic field (B_0) was shimmed and RF field (B_1) was calibrated. Image readout was single-slice, single-shot spin-echo (SE) echo planar imaging (EPI), (slice thickness = 3 mm, field of view 32 × 32 mm and imaging matrix 64 × 64, TR = 15,000 ms, TE = 20 ms). The B_0 map was obtained by acquiring six phase images with off-centered echo times (τ) of 0.25, 0.5, 1, 1.75, 2.5 and 3 ms. The B_1 map was quantified following the double angle method (DAM) proposed by Stollberger et al., with excitation angles of 60° and 120° (TR=15,000 ms, NA=4) (29). T_1 images were acquired using an inversion recovery sequence with eight inversion intervals (TI) from 100 to 6,000 ms (NA=2). The T_2 map was derived from five separate spin-echo images with echo times of 30, 40, 50, 60 and 80 ms (TR = 15,000 ms, NA=2). Z-spectra were acquired with interleaved CW- and pulsed-CEST imaging, and the irradiation RF power was systematically varied from 3.9 to 0.3 μT. Specifically, the irradiation pulse for pulsed-CEST imaging was chosen as an inversion pulse, with durations of 3, 5, 8, 10, 12, 14, 17, 20, 25 and 40 ms, and their corresponding RF powers are 3.9, 2.3, 1.5, 1.2, 1.0, 0.8, 0.7, 0.6, 0.5 and 0.3 μT, respectively. The equivalent RF power is derived according to,

NIH-PA Author Manuscript

NIH-PA Author Manuscript

NIH-PA Author Manuscript

$$B_{cw}=\frac{1}{\gamma\left(\tau_p+\tau_d\right)}\int_0^{\tau_p}\gamma B_1\,(t)\,dt \quad (1)$$

where γ is the gyromagnetic ratio, B_{cw} is the RF power for CW irradiation, τ_p and τ_d are the duration for each labeling RF pulse and the interpulse delay (Fig. 1), and $B_1(t)$ is the waveform for the Gaussian pulse. The RF frequency offsets were between ± 1,500 Hz (± 3.75 ppm at 9.4 T), with a frequency interval of 50 Hz (0.125 ppm at 9.4 T). Given that the longitudinal relaxation time of the tissue-like pH phantom has been found to be approximately 3 s at 9.4T, a long irradiation/saturation RF pulse is chosen in order to reach the steady state of CEST imaging. Specifically, the number of RF pulses was varied so that the total saturation time (TS) was 7.5 s (TR = 15,000 ms, TS = 7,500 ms, NA=2).

A quadruple pH phantom and normal human volunteers were imaged on a 3T Siemens Magnetom TIM Trio scanner (Siemens Medical Solutions, Erlangen, Germany). A body transmitter and a 12-channel head coil receiver were used concurrently to obtain homogeneous B_1 field and high detection sensitivity. For the phantom study, the B_0 field was shimmed using an in-house-developed B_0 shimming module that adjusts high-order gradient shimming currents based on the derived B_0 field map. An RF pulse train containing repetitive Gaussian inversion pulses was used for pulsed-CEST imaging, with an RF duty cycle of 50%. Crusher gradients with alternated polarity were applied between RF pulses in order to suppress residual transverse magnetizations. The inversion pulse duration was 20 ms, equivalent to mean RF power of 0.6 μT (single shot EPI, slice thickness = 10 mm, field of view 180 × 180 mm and image matrix 64 × 64, TR=6,000 ms, TS=3,000 ms, TE= 36 ms, NA=16). For MRI of normal human volunteers, APT, T_1-weighted, T_2-weighted and fluid-attenuated inversion recovery (FLAIR) scans were performed (slice thickness = 10 mm, FOV = 200 × 200 mm) with the same experimental setup. The TR and TE were 440 ms and 2.46 ms, respectively for T_1-weighted imaging (matrix size 64×64). For T_2-weighted MRI, TR and TE were 6,000 ms and 82 ms (matrix size=128×128), respectively. For FLAIR imaging, TR and TE were 8,000 ms and 85 ms (matrix size 128 × 128), respectively, with an inversion recovery delay of 2,500 ms. For APT imaging (TR=9,000 ms, TS=3,000 ms, NA= 8, matrix size=64×64), the inversion pulse duration was 20 ms, equivalent to an RF power of 0.6 μT, with an RF duty cycle of 50%. The RF offset was swept between ± 894 Hz (±7 ppm at 3 T), with a frequency interval of 64 Hz (0.5 ppm at 3 T). In addition, lipid suppression was applied prior to image acquisition to remove lipid artifacts and the scan time was approximately 30 minutes (30). The MTR asymmetry image was derived by subtracting the label scan (3.5 ppm) from the reference image (-3.5 ppm), and normalized by the control scan as (8),

$$MTR_{asym}=\frac{I_{ref}-I_{lable}}{I_{control}}\times 100\% \quad (2)$$

where I_{ref} and I_{label} are the reference and label image, with irradiation RF pulse applied at the reference and labile proton frequency, respectively, and $I_{control}$ is the control scan without irradiation pre-pulse. It is worthwhile to note that for a 2-pool exchange model of bulk water and labile protons, we have MTR_{asym}=CESTR. When amide groups are probed such as the endogenous APT MRI, APT ratio (APTR) is often used to specify its amide proton origin.

NIH-PA Author Manuscript

NIH-PA Author Manuscript

NIH-PA Author Manuscript

3. RESULTS

CW and pulsed-CEST imaging pulse sequences are shown in Fig. 1. For CW-CEST imaging (scheme a), an RF pulse is applied for a duration comparable to the bulk water relaxation time, typically a few seconds, followed by a fast readout such as EPI. For pulsed CEST imaging (scheme b), the CW irradiation module is replaced by repetitive RF pulses of duration (τ_p), with an inter-pulse delay of τ_d. During the inter-pulse delay, bipolar crusher gradients can be applied to suppress residual transverse magnetizations and minimize echo formation from neighboring RF pulses.

Fig. 2a shows three z-spectra acquired from the triple-pH phantom with CW irradiation at 9.4 T (B_1 = 1 μT). The pH-dependent CEST contrast can be observed at the labile amine protons frequency of 1.9 ppm. It is so because the relaxation rates and semisolid macromolecular content were equal among the three compartments, while their amine proton exchange is different due to pH titration. The z-spectra were concurrently fit using a 3-pool exchange model modified from that of Woessner et al. (26). Whereas the original routine has been used to simulate CEST imaging of two labile groups, the modified simulation routine evaluated one labile group from mobile proteins/peptides with the second exchange group for conventional MT effects from semisolid macromolecules. As such, the exchange rate, chemical shift offset, and relaxation rates for the second pool are similar as those found from the conventional MT. In addition, identical relaxation and concentration parameters were used for three pH compartments, while the chemical exchange rate was set as an independent parameter for each compartment. Longitudinal relaxation time for bulk water, amine protons and semisolid macromolecules was set to be 3 s, 1 s and 1 s, as obtained previously (25,28). In addition, the transverse relaxation time for semisolid macromolecules was assumed to be 15 μs (31-33). As such, there were eight unknown parameters to be determined: transverse relaxation time for bulk water (T_{2w}) and amine protons (T_{2s}), the concentration for labile amine group (f_s) and semisolid macromolecules (f_{MT}), conventional MT exchange rate (k_{MT}), and three proton exchange rates (k_{sw1}, k_{sw2} and k_{sw3}). In Fig. 2a, blue, green and red lines represent numerical fitting for pH of 5.2, 6.0 and 6.4, respectively, in good agreement with the experimentally obtained z-spectra. The corresponding chemical exchange rate was found to be 25 s^{-1}, 57 s^{-1} and 85 s^{-1}, respectively, while their T_1 and T_2 were found to be approximately equal (Table 1). In addition, the amine proton concentration was found to be 1:779, with a transverse relaxation time of 11 ms, and the transverse relaxation time for bulk water was obtained to be 47 ms. It is important to point out that the chemical exchange rate and amine proton concentration is comparable to those found from in vivo APT imaging, hence making the studied phantom a reasonable model to investigate in vivo APT MRI (8,10,34). Moreover, the semisolid macromolecular content and exchange rate was 1:42 and 50 s^{-1}, respectively. Fig. 2b shows an illustration of the triple-gel phantom and two CEST maps using CW- and pulsed-CEST imaging at 9.4T (B_1=0.8 μT). The CESTR obtained with CW irradiation was 3.6 ± 0.9%, 11.0 ± 1.0% and 14.6 ± 1.3% for pH of 5.2, 6.0 and 6.4, respectively. In comparison, the pulsed-CEST imaging showed a corresponding CEST contrast of 3.8 ± 1.3%, 10.0 ± 1.2% and 13.7 ± 1.4%, respectively. It is worth noting that there is a minor pulsed-CEST contrast decrease of (~1%) for pH of 6.0 and 6.4, which can be attributed to reduced labeling coefficient for amine groups of faster chemical exchange rates.

Fig. 3a compares the CEST contrast obtained with CW- and pulsed-CEST imaging. The CEST contrast initially increased with RF irradiation power and reached maximal values when irradiation power was between 0.8 and 1 μT (Fig. 3a). For even higher RF powers, the CEST contrast decreased as a result of concomitant RF irradiation effects (25). The CEST contrast between pH compartments of 6.0 and 5.2, 6.4 and 6.0, and 6.4 and 5.2 is shown in Fig. 3 b, c, and d, wherein solid black and light gray marks represent the CW- and pulsed-

NIH-PA Author Manuscript

NIH-PA Author Manuscript

NIH-PA Author Manuscript

CEST contrast, respectively. It shows that the optimal RF power for CW- and pulsed-CEST imaging is approximately equal, which is consistent with the fact that amine proton transfer investigated in this study is within the range of slow to intermediate exchange. As such, a moderate irradiation RF power of 1 μT can sufficiently label the exchangeable protons with minimal spillover effects.

Shown in Fig. 4 are an illustration of the quadruple-pH phantom, a control MRI scan (without RF irradiation), and pulsed-CESTR map. The phantom contains four compartments; three are Creatine-Agarose gel mixture titrated at pH of 6.5, 5.9 and 5.3, clockwise from top to bottom, respectively. The leftmost compartment is a 50 mM Creatine solution at pH of 5.8. The gel phantom in the control scan appeared hypointensive in comparison to both the creatine solution compartment and the exterior $CuSO_4$ solution, as gel mixture has T_2 values much shorter than that of solution state. However, the difference in relaxation time alone is not sufficient to differentiate the compartmental pH of creatine-agarose gel mixture. In contrast, CESTR was found to be 1.5 ± 0.2%, 2.5 ± 0.3% and 3.6 ± 0.4% for pH of 5.3, 5.9 and 6.5, respectively. It is interesting to note that the CESTR for creatine solution (pH=5.8) was 10.2 ± 0.7%, even greater than that from the creatine gel phantom at higher pH of 6.5. It is so because the transverse relaxation time of the creatine solution compartment is significantly longer than those of gel-based phantoms, and thus less susceptible to RF spillover effects.

Fig. 5 compares pulsed-CEST contrast obtained at 9.4 T (circle) versus that derived from 3 T (square). For the pH range and RF power investigated in this study, CESTR increased almost linearly with pH, consistent with the conclusion that amine proton exchange is dominantly base-catalyzed. It is important to note that the CESTR-pH slope at 3 T is 2% per pH unit, while it is 8% per pH unit at 9.4T. It is so because the labile amine group is only 1.9 ppm from bulk water resonance, which is equivalent to 240 Hz at 3T, and 760 Hz at 9.4T. As such, CEST imaging is less susceptible to spillover effects at 9.4T than at 3T, and consequently, a higher RF labeling pulse can be used for more efficient saturation of exchangeable protons. In addition, the longer longitudinal relaxation time at higher field also contributes to the higher CEST contrast measured at 9.4T.

Fig. 6 shows T_1-W, T_2-W, FLAIR and APT images from a representative normal volunteer. The MTR asymmetry (MTR_{asym}) in brain white matter (WM) is lower than that of grey matter (GM) and cerebral spinal fluid (CSF), similar as those previously observed from APT imaging of animals (8,10,21). Given that our preliminary human APT images have relatively coarse spatial resolution, brain GM could not be outlined for quantitative comparison with that of previous animal APT imaging. However, the APTR of ROI chosen within brain WM was found to be - 4.2 ± 0.2%. In addition, APTR of cerebral spinal fluid (CSF) was found to be - 0.15% from a subject whose MRI clearly captured the ventricle body. It is consistent with the finding of Zhou et al. that Z-spectrum for ventricle is nearly symmetric around bulk water resonance, and thus the CESTR for CSF is approximately zero (8). Given that under optimal experimental condition, the APTR contrast between normal and ischemic tissue is expected to be about 3%, our pilot data strongly suggest that the sensitivity of pulsed-APT imaging at 3 Tesla is sufficient to detect tissue acidosis in clinic. As a result, our study warrants future APT imaging of stroke patients to evaluate the diagnostic value of pH-weighted APT imaging.

4. DISCUSSION

In this study, we showed that that the optimal RF power and maximal CEST contrast from pulsed-CEST imaging is comparable with those of CW-CEST imaging, and the pulsed-CEST imaging can indeed detect pH contrast from tissue-like pH phantoms. Moreover, pilot

NIH-PA Author Manuscript

NIH-PA Author Manuscript

NIH-PA Author Manuscript

APT imaging of normal volunteers at 3 Tesla demonstrates the feasibility of pulsed-APT imaging at clinical field strengths, and warrants future evaluation of its diagnostic value in stroke patients. By interpolating our results of amine exchange (1.9 ppm) at 3T and 9.4T, we estimated that the pH-dependent APT imaging contrast (3.5 ppm) should be about 4% per pH unit at 3 T. Such an estimation is in line with our *in vivo* experiments at 4.7T that showed a 2.9% APT contrast for a pH change of about 0.6 unit (i.e., 5% per pH unit) (8,10). In order to model conventional MT effects incurred in biological tissue, we added Creatine to 3% Agarose Gel, similar to MT phantoms previously used by Graham and Henkelman (31). The labile proton and bulk water proton ratio obtained by numerical fitting of three Z-spectra concurrently was 1:779, in good agreement with previously reported result from fitting a single Z-spectrum (1:742) (28). In fact, the labile amide proton content for 50 mM Creatine has been estimated to be within 1:1100 and 1:455 by interpolating the results of Andrasco, with a mean concentration of 1:778 (28,35). On the other hand, it is important to point out that amine protons of creatine resonate at 1.9 ppm downfield from bulk water resonance, much closer than that of the composite endogenous labile amide protons (3.5 ppm), making the pH phantom used in this study susceptible to more concomitant RF irradiation effects than *in vivo* APT imaging. However, the fact that we can detect pH difference of 0.6 units using amine labile groups of smaller chemical offset from bulk water strongly suggests the feasibility of using endogenous amide proton transfer at 3.5 ppm to detect abnormal tissue pH during stroke. It is worth noting that CEST imaging is susceptible to magnetic field inhomogeneity (i.e., B_0 and B_1), which may need to be corrected for imaging at high-field scanners with unsatisfactory B_0 homogeneity. Such artifacts may become particularly challenging for imaging stroke patients, where the duration of MRI scans has to be kept minimal in order not to delay potential treatment. In order to address this issue, we have recently proposed an algorithm that compensates for moderate field inhomogeneity-induced CEST imaging artifacts, which may be applied if validated for in vivo APT imaging (28). In addition, given that APT imaging is a differential imaging technique in that it subtracts the normalized label scan from a reference scan, it is susceptible to motion artifacts. Such artifacts can be severe for stroke patients who may not hold still during the scan. In order to address this concern, we propose to acquire MRI data frame by frame, and signal averaging will be performed in post-processing after motion correction.

It is important to note that in addition to pH-dependent exchange process, the CEST contrast also varies with the relaxation constants and proton concentrations of the bulk water and labile groups. Given that the labile protons are often dilute and subject to slow to intermediate chemical exchange, the bulk water T_1 and T_2 can be directly measured. It is known that relaxation time varies with tissue type and the magnetic field strength, but the T_1 and T_2 of cerebral tissue are typically within 1.5-3 s and 50-100 ms, respectively (32). Because the longitudinal relaxation rate for labile protons is significantly less than its chemical exchange rate, it should only minimally affect the steady state of CEST contrast. Moreover, the labile proton T_2 can be obtained from either numerical fitting or experimental measurement (5,28). Furthermore, for certain applications of CEST MRI such as endogenous APT imaging of acute ischemic tissue acidosis, the relaxation rates, proton content and conventional MT imaging contrast have negligible changes during the initial few hours after stroke onset, and thus, should not affect the CEST imaging contrast (10,36). In Fig. 3, minor variation among three z-spectra at frequencies other than that of the amine group can also be observed, which can be attributed to minor B_1 inhomogeneity induced artifacts. Although RF spillover and conventional MT effects are susceptible to B_1 field inhomogeneity, CEST contrast has been shown to be relatively insensitive to B_1 field errors, as MTR asymmetry analysis can partially compensate for errors introduced by minor B_1 field inhomogeneity (25,28). In addition, B_0 field in human brain is often reasonably homogeneous, with a typical full width half maximum (FWHM) of about 15-20 Hz.

NIH-PA Author Manuscript

NIH-PA Author Manuscript

NIH-PA Author Manuscript

Moreover, our approach of concurrently fitting three z-spectra rather than fitting separately reduced the total number of fitting parameters, making our numerical fitting less susceptible to uncertainties of multi-parameter non-linear fitting. The observation that pH-induced Z-spectra contrast is dominantly around the labile proton frequency is consistent with those reported by Makela et al. that during acute stroke, the conventional MT and relaxation rates have insignificant change (36). In fact, the obtained parameters agreed reasonably well with our previous results of similar creatine-gel phantoms from fitting z-spectra across a broad range of RF irradiation powers, suggesting that our obtained parameters should provide reasonably accurate description of the investigated system (28). In addition, it is helpful to make a brief comparison of pulsed-CEST and MT imaging (37,38). The transverse relaxation time for semisolid macromolecules is very short, with its spectral width typically on the order of 100 kHz. As such, it takes a strong RF irradiation pulse applied at very large offsets to produce selective saturation of semisolid macromolecules for MT imaging. In contrast, the T_2 for labile protons is on the order of tens of ms, indicating that irradiation pulses with a narrow excitation bandwidth should be chosen for CEST imaging in order to minimize spillover effects. In addition, unlike conventional MT imaging, where both offset and power for irradiation RF can be varied for optimization, the RF offset for CEST imaging is fixed because mobile labile protons usually have a well defined, narrow spectrum. Moreover, it is known that conventional semisolid macromolecular MT imaging is not sensitive to pH difference, while by selectively saturating pH-dependent exchangeable protons, the CEST imaging can easily detect minor pH contrast, as shown in this study.

Although our current study explored pulsed-CEST imaging of repetitive inversion pulse for CEST imaging, it is expected that RF pulses with other flip angles such as 90° should reach similar steady state, provided that it has equivalent RF irradiation power. It is important to point out that in our preliminary APT imaging reported in this work, the in-plane resolution and slice thickness were chosen to maximize the signal to noise ratio (SNR) for the purpose of validating the imaging technique. The fact that the variance of APTR across subjects was relatively small (0.2%) suggests that the spatial resolution can be increased without significant deterioration of SNR. Finally, although it is known that diseases such as stroke and cancer are spatially heterogeneous, we only explored single-slice APT imaging in the current study. As a result, fast volumetric APT imaging has to be developed and validated before it can become a routine clinical scan. It is worthwhile to mention that we have recently proposed a relaxation-compensated fast multi-slice APT imaging technique and it will be adopted on the 3 Tesla for the upcoming APT imaging (39).

5. CONCLUSION

In this study, we compared pulsed- and CW-CEST imaging and showed that the optimal RF power and maximal CEST contrast for both irradiation schemes are approximately equal. Moreover, we translated pulsed-CEST imaging to a 3T clinical scanner and demonstrated CEST imaging of a tissue-like pH phantom and normal human volunteers. Further study of pH-weighted APT imaging of acute stroke patients is necessary to elucidate its diagnostic value for characterizing ischemic tissue damage and guiding stroke therapeutics.

Acknowledgments

This study was supported in part by grants from NIH/NINDS 5R01NS038477-09 and NIH/NCRR P41RR14075. We would like to thank Dr. Peter van Zijl and Dr. Jinyuan Zhou from Johns Hopkins University for helpful discussions, and Dr. Timothy Reese for help with magnetic shimming on the 3 Tesla Siemens scanner. We also would like to acknowledge Dr. Donald Woessner and Dr. Dean Sherry from University of Texas at Dallas for kindly sharing with us their MATLAB simulation routines.

NIH-PA Author Manuscript

NIH-PA Author Manuscript

NIH-PA Author Manuscript

REFERENCES

1. Wolff SD, Balaban RS. NMR imaging of labile proton exchange. J Magn Reson. 1990; 86:164–169.
2. Zhang S, Winter P, Wu K, Sherry AD. A novel europium(III)-based MRI contrast agent. J Am Chem Soc. 2001; 123(7):1517–1578. [PubMed: 11456734]
3. Aime S, Delli Castelli D, Fedeli F, Terreno E. A paramagnetic MRI-CEST agent responsive to lactate concentration. J Am Chem Soc. 2002; 124(32):9364–9365. [PubMed: 12167018]
4. van Zijl PCM, Zhou J, Mori N, Payen J, Mori S. Mechanism of magnetization transfer during on-resonance water saturation. a new approach to detect mobile proteins, peptides, and lipids. Magn Reson Med. 2003; 49:440–449. [PubMed: 12594746]
5. McMahon M, Gilad A, Zhou J, Sun PZ, Bulte J, van Zijl PC. Quantifying exchange rates in chemical exchange saturation transfer agents using the saturation time and saturation power dependencies of the magnetization transfer effect on the magnetic resonance imaging signal (QUEST and QUESP): Ph calibration for poly-L-lysine and a starburst dendrimer. Magn Reson Med. 2006; 55(4):836–847. [PubMed: 16506187]
6. Ward KM, Balaban RS. Determination of pH using water protons and chemical exchange dependent saturation transfer (CEST). Magn Reson Med. 2000; 44:799–802. [PubMed: 11064415]
7. Sun PZ, Sorensen AG. Imaging pH using the Chemical Exchange Saturation Transfer (CEST) MRI: Correction of Concomitant RF Irradiation Effects to Quantify CEST MRI for Chemical Exchange Rate and pH. Magn Reson Med. 2008 in press.
8. Zhou J, Payen J, Wilson DA, Traystman RJ, van Zijl PCM. Using the amide proton signals of intracellular proteins and peptides to detect pH effects in MRI. Nature Med. 2003; 9:1085–1090. [PubMed: 12872167]
9. Jokivarsi KT, Gröhn HI, Gröhn OH, Kauppinen RA. Proton transfer ratio, lactate, and intracellular pH in acute cerebral ischemia. Magn Reson Med. 2007; 57(4):647–653. [PubMed: 17390356]
10. Sun PZ, Zhou J, Huang J, van Zijl P. Simplified Quantitative Description of Amide Proton Transfer (APT) Imaging During Acute Ischemia. Magn Reson Med. 2007; 57(2):405–410. [PubMed: 17260362]
11. Warach S. Measurement of the Ischemic Penumbra With MRI: It's About Time. Stroke. 2003; 34(10):2533–2534. [PubMed: 12970511]
12. Albers G, Thijs VN, Wechsler L, Kemp S, Schlaug G, Skalabrin E, Bammer R, Kakuda W, Lansberg MG, Shuaib A, Coplin W, Hamilton S, Moseley M, Marks MP, the Defuse Investigators. Magnetic resonance imaging profiles predict clinical response to early reperfusion: The diffusion and perfusion imaging evaluation for understanding stroke evolution (DEFUSE) study. Ann Neurol. 2006; 60(5):508–517. [PubMed: 17066483]
13. Gonzalez RG. Imaging-Guided Acute Ischemic Stroke Therapy: From "Time Is Brain" to "Physiology Is Brain". AJNR Am J Neuroradiol. 2006; 27(4):728–735. [PubMed: 16611754]
14. Kidwell C, Saver J, Mattiello J, Starkman S, Vinuela F, Duckwiler G, Gobin Y, Jahan R, Vespa P, Kalafut M, Alger J. Thrombolytic reversal of acute human cerebral ischemic injury shown by diffusion/perfusion magnetic resonance imaging. Ann Neurol. 2000; 47(4):462–469. [PubMed: 10762157]
15. Ringer TM, Neumann-Haefelin T, Sobel RA, Moseley ME, Yenari MA. Reversal of Early Diffusion-Weighted Magnetic Resonance Imaging Abnormalities Does Not Necessarily Reflect Tissue Salvage in Experimental Cerebral Ischemia. Stroke. 2001; 32(10):2362–2369. [PubMed: 11588327]
16. Tomlinson FH, Anderson RE, Meyer FB. Acidic foci within the ischemic penumbra of the New Zealand white rabbit. Stroke. 1993; 24(12):2030–2039. [PubMed: 8248985]
17. Hossmann KA. Viability thresholds and the penumbra of focal ischemia. Ann Neurol. 1994; 36(4): 557–565. [PubMed: 7944288]
18. Hata R, Mies G, Wiessner C, Fritze K, Hesselbarth D, Brinker G, Hossmann K-A. A Reproducible Model of Middle Cerebral Artery Occlusion in Mice: Hemodynamic, Biochemical, and Magnetic Resonance Imaging. J Cereb Blood Flow Metab. 1998; 18(4):367–375. [PubMed: 9538901]
19. Grohn OHJ, Lukkarinen JA, Oja JME, van Zijl PCM, Ulatowski JA, Traystman RJ, Kauppinen RA. Noninvasive Detection of Cerebral Hypoperfusion and Reversible Ischemia From Reductions

NIH-PA Author Manuscript

NIH-PA Author Manuscript

NIH-PA Author Manuscript

in the Magnetic Resonance Imaging Relaxation Time, T2. J Cereb Blood Flow Metab. 1998; 18(8):911–920. [PubMed: 9701353]

20. Kidwell C, Alger J, Saver J. Evolving paradigms in neuroimaging of the ischemic penumbra. Stroke. 2004; 35(11 Suppl 1):2662–2665. [PubMed: 15472112]
21. Sun PZ, Zhou J, Sun W, Huang J, van Zijl PCM. Detection of the ischemic penumbra using pH-weighted MRI. J Cereb Blood Flow Metab. 2007; 27(6):1129–1136. [PubMed: 17133226]
22. Forsen S, Hoffman RA. Study of moderately rapid chemical exchange reactions by means of nuclear magnetic double resonance. J Chem Phys. 1963; 39:2892–2901.
23. Zhou J, Wilson DA, Sun PZ, Klaus JA, van Zijl PCM. Quantitative description of proton exchange processes between water and endogenous and exogenous agents for WEX, CEST, and APT experiments. Magn Reson Med. 2004; 51:945–952. [PubMed: 15122676]
24. Zhou J, van Zijl PCM. Chemical Exchange Saturation Transfer Imaging. Progress in Nuclear Magnetic Resonance Spectroscopy. 2006; 48:109–136.
25. Sun PZ, van Zijl PCM, Zhou J. Optimization of the irradiation power in chemical exchange dependent saturation transfer experiments. J Magn Reson. 2005; 175(2):193–200. [PubMed: 15893487]
26. Woessner DE, Zhang S, Merritt ME, Sherry AD. Numerical solution of the Bloch equations provides insights into the optimum design of PARACEST agents for MRI. Magn Reson Med. 2005; 53(4):790–799. [PubMed: 15799055]
27. Siesjo BK. Pathophysiology and treatment of focal cerebral ischemia: Part I: Pathophysiology. J Neurosurg. 1992; 77(2):169–184. [PubMed: 1625004]
28. Sun PZ, Farrar CT, Sorensen AG. Correction for artifacts induced by B0 and B1 field inhomogeneities in pH-sensitive chemical exchange saturation transfer (CEST) imaging. Magn Reson Med. 2007; 58(6):1207–1215. [PubMed: 17969015]
29. Stollberger R, Wach P. Imaging of the active B1 field in vivo. Magn Reson Med. 1996; 35(2):246–251. [PubMed: 8622590]
30. Sun PZ, Zhou J, Sun W, Huang J, van Zijl PCM. Suppression of lipid artifacts in amide proton transfer imaging. Magn Reson Med. 2005; 54(1):222–225. [PubMed: 15968669]
31. Henkelman RM, Huang X, Xiang Q-S, Stanisz GJ, Swanson SD, Bronskill MJ. Quantitative interpretation of magnetization transfer. Magn Reson Med. 1993; 1993:759–766. [PubMed: 8350718]
32. Stanisz GJ, Odrobina EE, Pun J, Escaravage M, Graham SJ, Bronskill MJ, Henkelman RM. T1, T2 relaxation and magnetization transfer in tissue at 3T. Magn Reson Med. 2005; 54(3):507–512. [PubMed: 16086319]
33. Morrison C, Henkelman RM. A model for magnetization transfer in tissues. Magn Reson Med. 1995; 33(4):475–482. [PubMed: 7776877]
34. Gilad AA, McMahon MT, Walczak P, Winnard PT, Raman V, vanLaarhoven HWM, Skoglund CM, Bulte JWM, van Zijl PCM. Artificial reporter gene providing MRI contrast based on proton exchange. Nat Biotech. 2007; 25(2):217–219.
35. Andrasko J. Water in agarose gels studied by nuclear magnetic resonance relaxation in the rotating frame. Biophys J. 1975; 15(12):1235–1243. [PubMed: 1203448]
36. Makela HI, Kettunen MI, Grohn OH, Kauppinen RA. Quantitative $T_{1\rho}$ and magnetic transfer magnetic resonance imaging of acute cerebral ischemia in the rat. J Cereb Blood Flow Metab. 2002; 22:547–558. [PubMed: 11973427]
37. Graham SJ, Henkelman RM. Understanding pulsed magnetization transfer. J Magn Reson Imaging. 1997; 7(5):903–912. [PubMed: 9307918]
38. Graham SJ, Henkelman RM. Pulsed magnetization transfer imaging: evaluation of technique. Radiology. 1999; 212:903–910. [PubMed: 10478264]
39. Sun PZ, Murata Y, Lu J, Wang X, Lo EH, Sorensen AG. Relaxation-compensated fast multi-slice amide proton transfer (APT) imaging of acute ischemia. Magn Reson Med. 2008; 59(5):1175–1182. [PubMed: 18429031]

NIH-PA Author Manuscript

NIH-PA Author Manuscript

NIH-PA Author Manuscript

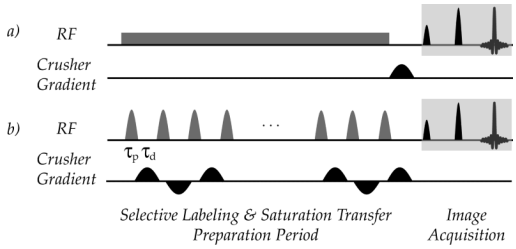

Figure 1.

NIH-PA Author Manuscript

NIH-PA Author Manuscript

NIH-PA Author Manuscript

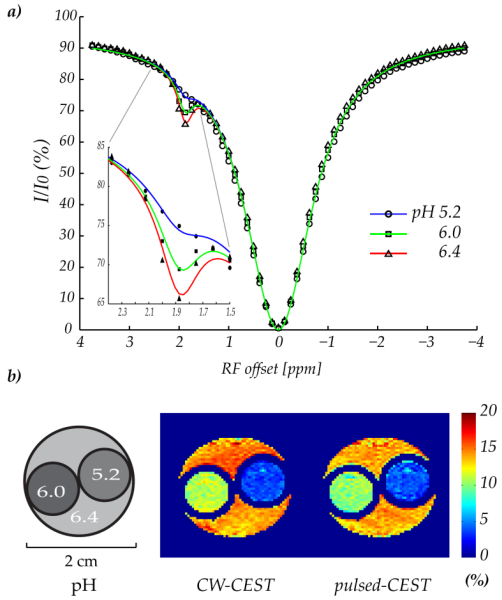

Figure 2.

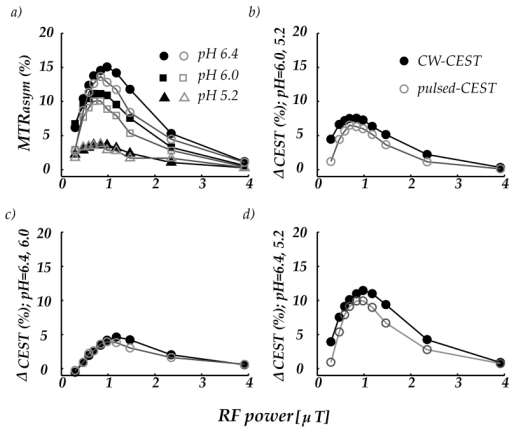

Figure 3.

NIH-PA Author Manuscript NIH-PA Author Manuscript NIH-PA Author Manuscript

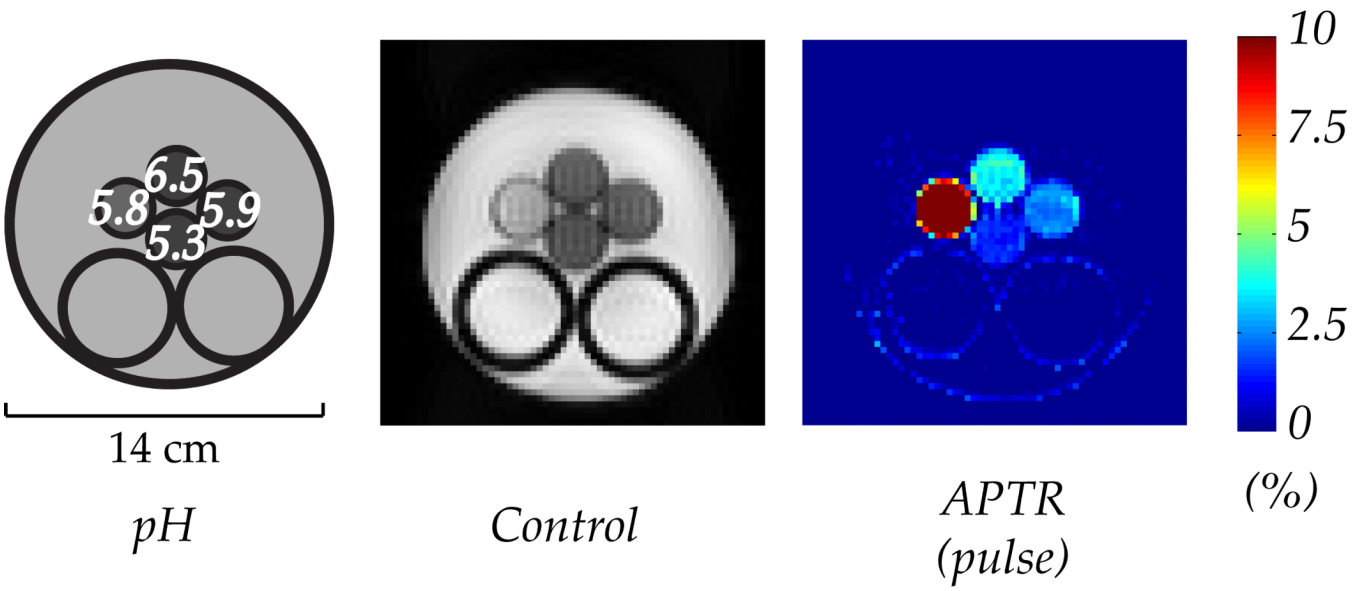

Figure 4.

NIH-PA Author Manuscript
NIH-PA Author Manuscript
NIH-PA Author Manuscript

NIH-PA Author Manuscript
NIH-PA Author Manuscript
NIH-PA Author Manuscript

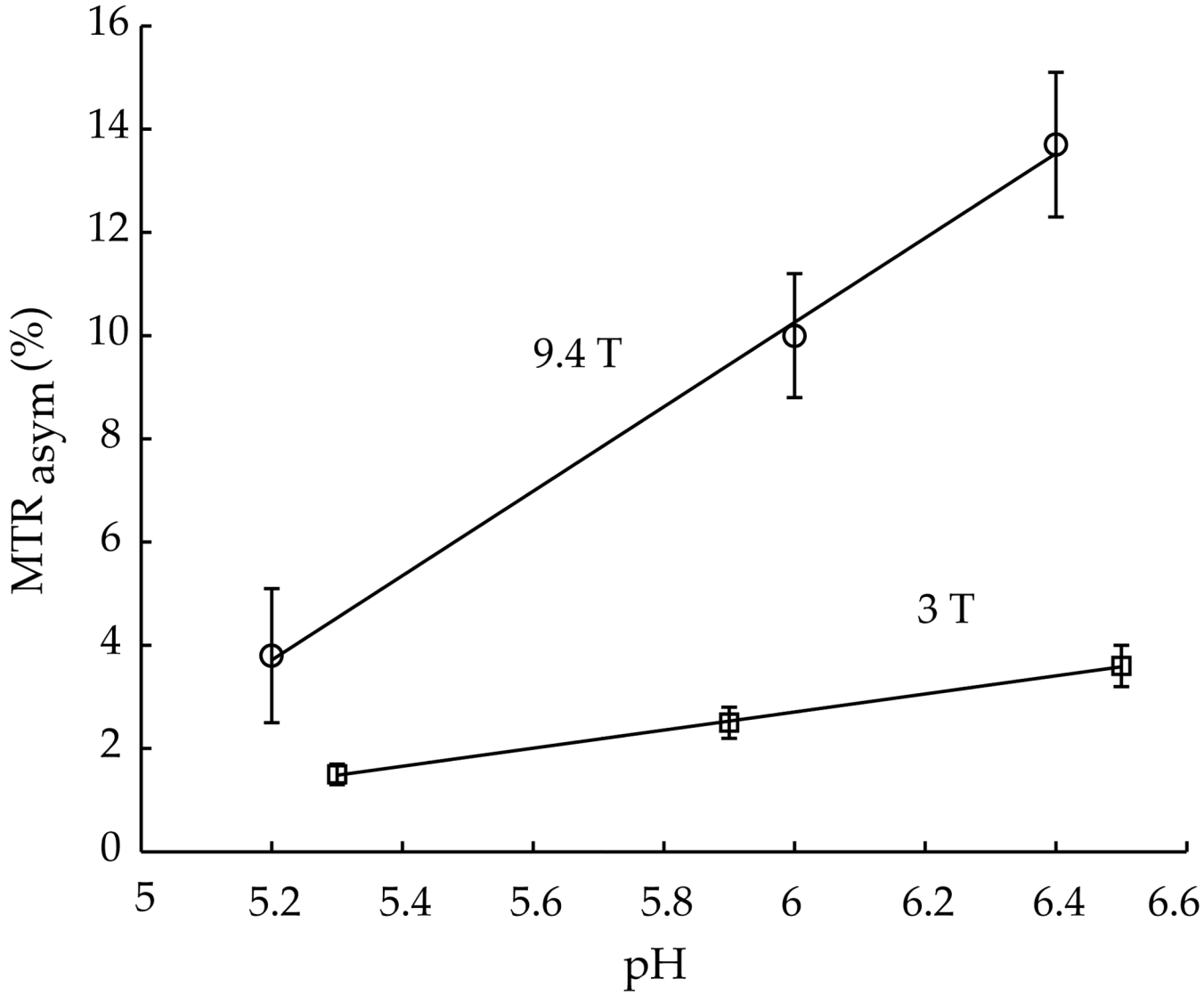

Figure 5.

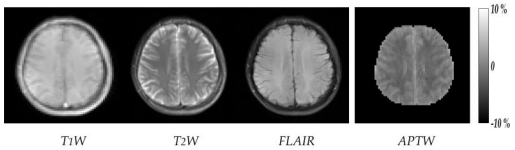

Figure 6.

NIH-PA Author Manuscript
NIH-PA Author Manuscript
NIH-PA Author Manuscript

NIH-PA Author Manuscript

NIH-PA Author Manuscript

NIH-PA Author Manuscript

Table 1

T_1, T_2 and MTR_{asym} measured for the triple-gel phantom containing 50 mM creatine and 3% Agarose titrated to pH values of 5.2, 6.0 and 6.4, respectively. Significant change in MTR_{asym} at 1.9 ppm was observed. Numerical fitting using a 3-pool chemical exchange model was applied to concurrently fit three z-spectra to characterize the properties of labile protons (Fig. 2a). The derived amine proton exchange rates (k_{sw}) were 25, 57 and 85 s^{-1}, respectively, and the concentration relative to bulk water proton was 1:779

pH	T_1 (s)	T_2 (ms)	MTR_{asym} (%) ($\Delta\omega$=750Hz, B_1=1 μT)	k_{sw} (s^{-1})
5.2	2.74 ± 0.05	40.8 ± 1.1	3.1 ± 1.0	25
6.0	2.76 ± 0.04	41.3 ± 1.2	9.9 ± 1.2	57
6.4	2.82 ± 0.04	40.9 ± 1.5	14.8 ± 1.1	85